Nano Research

Open Access

Research Article

Shape effect of prodrug nanoassemblies on treatment efficacy of cancer therapy

Fengxiang Liu[1,§], Rongzheng Liu[1,§], Xiaoyuan Fan[2,§], Xia Wang[2,§], Kaiyuan Wang[1,§], Hainan Zhao[3,§], Hao Ye[4], Shunzhe Zheng[1], Xiao Kuang[1], Yinxian Yang[1], Haotian Zhang[5], Qiming Kan[5], Zhonggui He[1,6], Jian Chen[7] ✉, and Jin Sun[1,6] ✉

[1] *Department of Pharmaceutics, Wuya College of Innovation, Shenyang Pharmaceutical University, Shenyang 110016, China*
[2] *School of Pharmacy, Shenyang Pharmaceutical University, Shenyang 110016, China*
[3] *Nephrology department, The First Affiliated Hospital of Jinzhou Medical University, Jinzhou 121000, China*
[4] *Multi-Scale Robotics Lab (MSRL), Institute of Robotics & Intelligent Systems (IRIS), ETH Zurich 8092, Switzerland*
[5] *School of Life Science and Biopharmaceutics, Shenyang Pharmaceutical University, Shenyang 110016, China*
[6] *Joint International Research Laboratory of Intelligent Drug Delivery Systems, Ministry of Education, Shenyang 110016, China*
[7] *School of Pharmacy, Shanghai Jiao Tong University, Shanghai 200240, China*
[§] *Fengxiang Liu, Rongzheng Liu, Xiaoyuan Fan, Xia Wang, Kaiyuan Wang, and Hainan Zhao contributed equally to this work.*

Cite this article: *Nano Research*, **2025**, *18*, 94907177. https://doi.org/10.26599/NR.2025.94907177

ABSTRACT: The tumor microenvironment-sensitive prodrug-based nanoparticles (NPs) have emerged as a promising drug delivery system (DDS). The shape of these particles plays a crucial role in their *in vivo* behavior. However, non-spherical organic NPs are rarely reported due to the inherent flexibility and variability of organic molecules. Herein, we fabricate reduction-sensitive prodrug NPs and explore the impact of their morphology properties on their *in vivo* fate. Prodrugs are self-assembled into spherical NPs with distearoyl phosphoethanolamine-PEG2000 (DSPE-PEG_{2K}), or into rod-shaped NPs with D-*α*-tocopherol polyethylene glycol 2000 succinate ($TPGS_{2K}$) due to the stronger binding energy. In comparison with spherical NPs, the endocytosis of rod-shaped NPs predominantly relies on caveolae-mediated pathways rather than clathrin-mediated ones, potentially avoiding degradation by lysosomes. Additionally, the rod-shaped NPs exhibit prolonged circulation time, increased tumor accumulation, and enhanced antitumor ability. Our current findings reveal the significant effect of particle shape on the behavior of prodrug NPs and introduce a novel paradigm for high-efficacy cancer therapy of prodrug NPs.

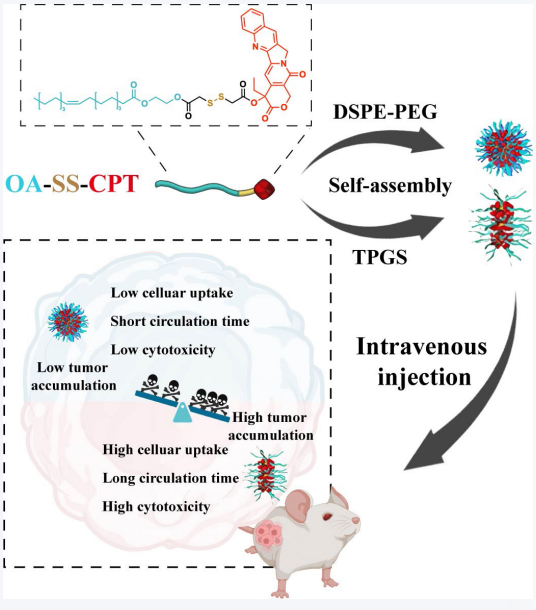

KEYWORDS: camptothecin, self-assembly, prodrug-based nanoparticles, nanorod, cancer therapy

1 Introduction

Among the clinical treatment modalities for cancer, chemotherapy remains a cornerstone, playing a crucial and irreplaceable role [1]. However, the clinical application of chemotherapeutic agents, such as camptothecin (CPT), a potent topoisomerase-1 inhibitor, is severely constrained by challenges like poor water solubility, high systemic toxicity, and non-specific distribution, which lead to suboptimal therapeutic efficacy and significant adverse effects [2, 3]. The limitations of traditional chemotherapy highlight an urgent need for innovative delivery strategies that enhance drug delivery precision, improve therapeutic outcomes, and mitigate systemic toxicity.

To address these limitations, a variety of drug delivery approaches have been designed [4–7]. The self-assembled prodrug

Received: September 28, 2024; **Revised:** November 26, 2024
Accepted: December 5, 2024

✉Address correspondence to Jian Chen, chenjian@sjtu.edu.cn; Jin Sun, sunjin@syphu.edu.cn

nanoparticles (NPs), which merge the features of approaches with nanotechnology-based delivery systems, stand out from numerous drug delivery systems (DDSs) [8]. In comparison with the common delivery systems such as nanocrystalline, liposomes, and micelles, self-assembled prodrug NPs simultaneously as drug carriers and active agents, which significantly enhances drug-loading capacity while reducing toxicity associated with carrier materials [9–11]. The prodrug strategy involves modifying the parent drug into an inactive form, which can then be converted back to the active drug *in vivo*, ensuring the safety of the drug. Self-assembled prodrug NPs further leverage this approach by offering enhanced tumor targeting, efficient cellular uptake, and extended circulation time [12, 13]. Moreover, the unique physicochemical characteristics of the tumor microenvironment (TME) make it possible for spatially specific drug release [14, 15]. By incorporating reduction-sensitive disulfide bonds, these customized NPs enable the on-demand release of chemotherapeutic agents specifically within the reductive regions, improving drug efficacy and minimizing off-target effects [16–18].

Recent studies have shown that the physical shape of NPs can profoundly impact their biological behavior, influencing critical aspects such as cellular uptake, biodistribution, circulation time, and immune system interactions [19]. While the size and surface properties of NPs are traditionally emphasized, emerging evidence suggests that shape also plays a crucial role in determining their fate within biological systems [20]. Although extensive research has been conducted on the morphological control of inorganic NPs with various non-spherical shapes, such as rods, discs, and stars, organic NPs, specially prodrug self-assembled NPs, have proven more challenging to shape due to the inherent flexibility and variability of organic molecules [21–25]. This limitation has led to a relatively poor understanding of how shape influences the therapeutic performance of organic NPs, particularly in terms of delivery efficiency and cellular interactions. Addressing these challenges in organic NP design could open new avenues for enhanced drug delivery and improved clinical outcomes in cancer therapy.

Herein, we constructed a reduction-responsive prodrug by conjugating CPT with oleic acid (OA) via a disulfide bond (CPT-2S-OA). As shown in Fig. 1, spherical NPs were self-assembled by CPT-2S-OA and distearoyl phosphoethanolamine-PEG2000 (DSPE-PEG_{2K}), while D-α-tocopherol polyethylene glycol 2000 succinate ($TPGS_{2K}$) contributed to the self-assembly of rod-shaped NPs due to the stronger binding energy. Further studies revealed that the internalization of spherical NPs mainly relied on clathrin-mediated endocytosis, whereas that of rod-shaped NPs was chiefly dependent on caveolae-mediated endocytosis, which improved uptake efficiency and cytotoxicity. Compared with DSPE-PEG_{2K}-modified spherical prodrug NPs, $TPGS_{2K}$-modified rod-shaped prodrug NPs exerted superior antitumor efficiency, benefiting from enhanced cellular uptake, extended circulation time, and increased tumor accumulation. Integrating a rod-shaped structure into disulfide bond-linked prodrug NPs provided a prototype for enhancing the cancer treatment efficacy of microenvironment-responsive prodrug NPs.

2 Experimental

2.1 Materials

CPT, $TPGS_{2K}$, and DSPE-PEG_{2K} were purchased from Aladdin (Shanghai, China). Trypsin-EDTA, 3-(4,5-dimethylthiazol-2-yl)-2,5-diphenyl tetrazolium bromide (MTT), coumarin-6 and DiR iodide were obtained from Dalian Meilun Biotechnology Co., Ltd (Dalian, China). 1-Ethyl-3-(3-dimethyllaminopropyl) carbodiimide hydrochloride (EDCI), hydroxybenzotriazole (HOBt), 4-dimethylaminopyrideine (DMAP), and p-toluene sulfonic acid were purchased from Energy Chemical (Shanghai, China).

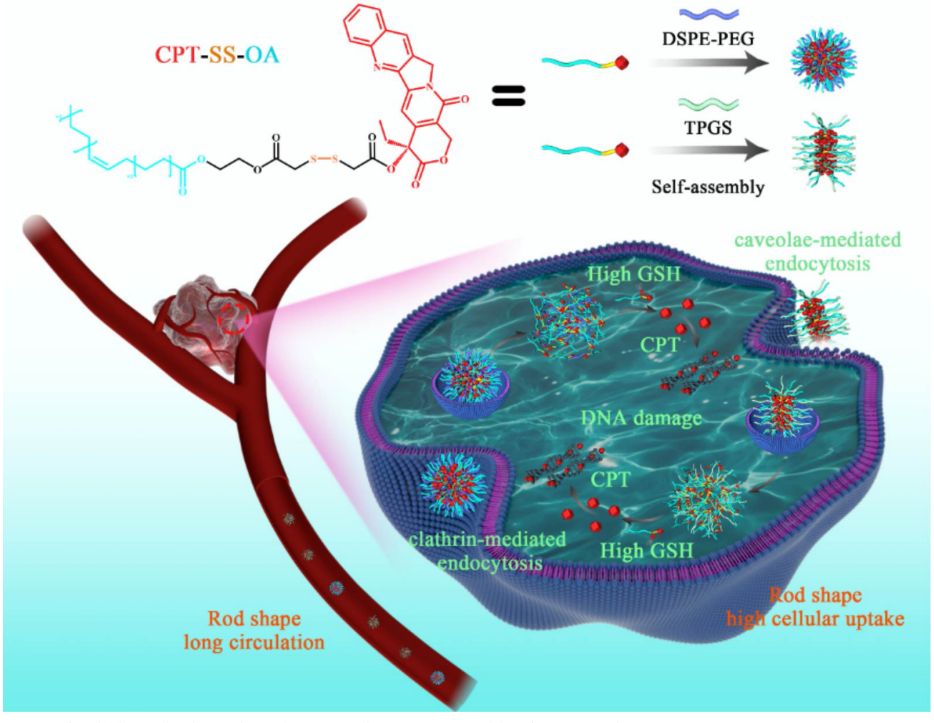

Figure 1 Schematic illustration of rod-like and sphere-shaped CPT prodrug nanoassemblies for cancer therapy.

Dithiodiglycolic acid was purchased from Aladdin (Shanghai, China). Hoechst 33342 was purchased from BD Biosciences (USA). Cell culture reagents were purchased from GIBCO, Invitrogen Corp (Carlsbad, California, USA). Other reagents and solvents involved in the experiment were of analytical grade.

2.2 Synthesis of CPT prodrugs

Ethylene glycol (15.3 mL) was mixed with p-toluene sulfonic acid (0.17 g) and oleic acid (0.84 g) and then stirred at 110 °C under nitrogen protection. The synthetic product was initially purified via extraction with methylbenzene and washing with $NaHCO_3$ solution, followed by further purification through column chromatography. Subsequently, CPT (0.25 g), HOBt (0.16 g), EDCI (0.25 g), and dithiodiglycolic acid (0.19 g) were dissolved in 20 mL of trichloromethane in an ice bath. The mixture was then allowed to react for 48 h at room temperature in a water bath. After the reaction, the synthetic product was leached with a NaCl solution and dried using a desiccant. The intermediate was further purified using column chromatography. Finally, EDCI (0.197 g), ethyl oleate, the intermediate (0.3 g), and DMAP (0.007 g) were dissolved in trichloromethane (20 mL). The catalyst was activated under 0 °C incubation conditions and then continuously stirred for 48 h at room temperature. Pure CPT-2S-OA was obtained through separation and purification using preparative liquid chromatography. The synthesis of CPT-2C-OA employed the same method.

2.3 Fabrication and characterization of CPT prodrug nanoparticles

The nanoprecipitation method was employed to directly fabricate prodrug NPs. In the PEGylation step, CPT-2S-OA prodrugs (or CPT-2C-OA prodrugs) were dissolved in a PEGylation solution consisting of acetone and $TPGS_{2K}$ (or DSPE-PEG_{2K}, comprising 20% of the prodrug weight). The solution was then added dropwise to stirring deionized water. Subsequently, the nano-formulation was subjected to rotary evaporation to remove the acetone. The size of the formulation was measured using dynamic light scattering (Malvern, UK). The values of zeta potential and the polydispersity index (PDI) were also determined using the same method. The morphology of the prodrug NPs was examined by transmission electron microscopy (TEM). To assess the colloidal stability of the formulation, mixtures containing the formulations and phosphate buffered solution (PBS) with 10% fetal bovine serum (FBS) solution (pH 7.4) were shaken at 37 °C. The size of the prodrug NPs was monitored over time using Malvern.

2.4 Assembly mechanisms and molecular simulations

For exploring the assembly mechanisms of prodrug NPs, the fluorescence and ultraviolet spectrum of CPT solution, CPT-2S-OA/DSPE-PEG_{2K} NPs, CPT-2S-OA NPs/$TPGS_{2K}$, CPT-2C-OA/DSPE-PEG_{2K} NPs, and CPT-2C-OA/$TPGS_{2K}$ NPs were acquired using the microplate reader (Thermo Scientific, USA). The interactions between two types of prodrug molecules and PEG molecules were investigated by treating prodrug nano-assemblies with a range of NaCl, sodium dodecyl sulfate (SDS), urea, or KCl at 37 °C for 2 h. The changes in particle size were recorded to analyze the intermolecular interactions.

Additionally, molecular simulations were further used to certify the driving interactions during the assembly process. The structures of prodrugs were created using Chemdraw software. The 3D structures of prodrugs were built by optimizing containing the structural minimization with Chem3D and ligand prepared with DS 2019. The interaction between TPGS and DSPE molecules and two prodrug molecules was predicted by molecular docking using CDOCKER of DS 2019 software. All parameters were maintained at the default values.

2.5 Drug release of CPT prodrug nanoparticles

The release profiles of CPT from prodrug NPs were evaluated using PBS (containing 30% ethanol) with varying concentrations of dithiothreitol (DTT) as the release medium. The formulation was incubated in the release media on a laboratory shaker at 37 °C. At predetermined time points, the release media was filtered through a 0.5 mm membrane and subsequently analyzed by high-performance liquid chromatography (HPLC).

2.6 Cell culture

CT26 cells were cultured in RPMI 1640 with 10% FBS and 1% penicillin/streptomycin. The environment was maintained in a humidified atmosphere at 37 °C.

2.7 Cellular uptake and pathways of endocytosis

For exploring the cellular uptake efficiency of prodrug NPs, CT26 cells were seeded in confocal dishes with culture medium and incubated for 24 h. Then, the culture solution was removed and the cells were incubated with free coumarin-6 solution or coumarin-6-labeled prodrug NPs for 0.5 or 2 h in a cell incubator. Following incubation, the medium containing the drugs was discarded, and the cells were washed three times with cold PBS and fixed with 4% formaldehyde for 10 min. Subsequently, the cells were re-washed with PBS and counterstained with Hoechst dye. Finally, the prepared dishes were observed by a confocal laser scanning microscopy (CLSM, TCS SP2/AOBS, LEICA, Germany).

For fluorescent quantifications, CT26 cells were cultured in 12-well plates at a density of 1×10^5 cells per well for 24 h. After incubation with free coumarin-6 solution or coumarin-6-labeled prodrug NPs for 0.5 or 2 h respectively, the cells were washed and resuspended in PBS. Intracellular fluorescence intensity was measured by an FACSCalibur flow cytometer.

To determine the endocytosis pathway of nanoparticles, CT26 cells were treated using the method described above. For the energy-dependent process, the cells were pre-cultured at 4 °C, then incubated with coumarin-6-labeled prodrug NPs (500 ng/mL, coumarin-6 equivalent), and cultured at 4 °C for 2 h. For the clathrin-mediated pathway, the cells were pre-treated in media supplemented with chlorpromazine (CPZ, 5 μg/mL) for 1 h, followed by incubation with media containing coumarin-6-labeled prodrug nano-assemblies and CPZ for another 2 h. For the caveolae-mediated pathway, the procedure was identical to the clathrin-mediated pathway, except CPZ was replaced with filipin (FLP). Intracellular fluorescence intensity was quantitatively assessed using flow cytometry and further examined by CLSM.

2.8 Cytotoxicity assays

MTT assay was utilized to examine the antitumor activities of CPT and prodrug NPs. For *in vitro* cytotoxicity testing with CT26 cells, the cells were seeded into 96-well plates at a density of 2×10^3 cells per well for 24 h. Then, the cell culture medium was replaced with CPT and various concentrations of prodrug NPs, and the cells were further incubated for 48 or 72 h. After reaching the preset incubation time, the medium containing the drugs was replaced

with MTT solution and the cells were incubated for an additional 4 h. Following incubation, the MTT solution was removed, and dimethyl sulfoxide (DMSO) was added to dissolve the formazan crystals formed. Finally, the absorbance was measured using a microplate reader to determine the cell viability after various treatments.

2.9 *In vivo* pharmacokinetics

Male Sprague-Dawley rats (210–240 g, n = 3) were selected as model animals for the pharmacokinetic study. The rats were fasted for 12 h in advance and injected intravenously with CPT or prodrug NPs (4 mg/kg of CPT equivalent). At the predetermined time points (0.08, 0.25, 0.5, 1, 2, 3, 4, 8, 12, and 24 h post-injection), the whole blood was collected from each rat to obtain plasma. Then, each 50 μL of plasma sample was mixed with 25 μL of tetra-n-butylammonium hydroxide solution (5%). After vortexing for 10 min, 150 μL of acetonitrile was added to the sample and then vortexed for another 3 min. After centrifugating, the concentration of CPT in the supernatant was subsequently measured using a microplate reader (Model 500, USA).

2.10 *In vivo* biodistribution

BALB/c mice bearing CT26 cells were selected as model animals for the biodistribution study of prodrug NPs [26]. After the volume of tumor made by subcutaneous injection of CT26 cells reached around 300 mm^3, free DiR and DiR-labeled formulation (1 mg/kg) were administrated intravenously. After injection, each group of mice was observed and photographed at specific time points (4, 8, 12, and 24 h). Subsequently, the fluorescence of major organs and tumors was obtained and quantified using an IVIS Lumina Imaging System.

Additionally, to assess the tumor penetration effect of various nanoparticles, CPT, CPT-2S-OA/DSPE-PEG_{2K}, and CPT-2S-OA/$TPGS_{2K}$ were intravenously injected into CT26 tumor-bearing mice. 24 h post-injection, tumors were excised and subjected to 4',6-diamidino-2-phenylindole (DAPI) staining. CPT fluorescence in tumor tissues was then observed using CLSM.

2.11 *In vivo* antitumor efficacy

BALB/c mice bearing CT26 cell-induced tumors were selected to evaluate the antitumor efficacy of prodrug NPs. Once the tumors reached a volume of approximately 100 mm^3 via subcutaneous injection of CT26 cells, CPT and prodrug NPs were administered intravenously at a dose of 2 mg/kg, every two days. The tumor volume and body weight of the mice were measured and recorded daily. Ten days after the first administration, the mice were sacrificed, and blood samples were collected for analysis. Tumor tissues and major organs, including the heart, liver, spleen, lung, and kidney, were fixed in 4% paraformaldehyde and subsequently stained with hematoxylin and eosin (H&E). Additionally, apoptosis in the tumor tissues was assessed using the terminal deoxynucleotidyl transferase–mediated deoxyuridine triphosphate nick end labeling (TUNEL) assay.

2.12 Statistical analysis

Data was displayed as mean ± standard deviation (SD). Comparison between groups was analyzed with one-way analysis of variance (ANOVA). All data were analyzed by GraphPad Prism 7. Statistical significance was indicated by $^*P < 0.05$, $^{**}P < 0.01$, $^{***}P < 0.001$, and $^{****}P < 0.0001$.

3 Results and discussion

3.1 Preparation and characterization of CPT-2S-OA and CPT-2C-OA

As shown in Fig. S1 in the Electronic Supplementary Materia (ESM), the reduction-responsive CPT prodrug (CPT-2S-OA) was synthesized by coupling oleic acid to CPT through a disulfide bond. The carbon bond-bridged CPT-2C-OA was constructed as a non-sensitive control for the disulfide bond. As illustrated in Figs. S2 and S3 in the ESM, the structures of CPT-2S-OA and CPT-2C-OA were confirmed using mass spectrometry (MS) and ^{1}H nuclear magnetic resonance (^{1}H NMR).

3.2 Fabrication and characterization of CPT prodrug NPs

In Table S1 in the ESM, both CPT–2S-OA and CPT-2C-OA prodrugs could self-assemble into stable NPs through a one-step nanoprecipitation process (Fig. 2(a)). The mean particle diameter of the rod-shaped prodrug NPs was 120 nm. The size of the spherical NPs was approximately 110 nm (Fig. 2(b)). TEM images exhibited that DSPE-PEG_{2K} NPs had a spherical morphology, whereas $TPGS_{2K}$ NPs displayed a rod-like structure (Fig. 2(c)). It also showed that rod-shaped prodrug NPs ranged in length from 100 to 160 nm and in width from 20 to 50 nm. The zeta potentials of CPT-2S-OA NPs and CPT-2C-OA NPs were around −20 mV. The drug loading efficiencies of all self-assembled NPs exceeded 40%.

We compared the colloidal stability of prodrug NPs without stabilizer addition. As shown in Fig. S4(a) in the ESM, in the absence of any stabilizer, the particle sizes of CPT-2S-OA and CPT-2C-OA increased significantly after incubation. This indicated that the self-assembly capability provided by the side chains alone was insufficient to maintain the stability of the prodrug NPs under the experimental conditions. Furthermore, the stability of CPT-2S-OA was slightly better than that of CPT-2C-OA, as it remained relatively stable for 4 h. In contrast, visible precipitation occurred within 4 h in CPT-2C-OA (Fig. S4(b) in the ESM). This can be attributed to the increased flexibility of the prodrug molecules due to the disulfide linkage, which introduced structural defects and enhanced the intrinsic assembly capability of CPT-2S-OA [8, 27].

Then, the stability discrepancy of prodrug NPs with 20% DSPE-PEG_{2K} or $TPGS_{2K}$ was observed when they were diluted in PBS (pH 7.4) containing 10% FBS. As shown in Fig. S4(c) in the ESM, the NPs exhibited minimal change in particle size over 24 h, indicating that the interactions between the drug molecules and stabilizers facilitated the formation of a more stable co-assembled structure. Notably, the introduction of the disulfide bond also enhanced the assembly performance of the prodrug NPs. The particle sizes of CPT-2S-OA/DSPE-PEG_{2K} and CPT-2S-OA/$TPGS_{2K}$ only increased slightly over 24 h.

Although the type of linker affected more on stability, the shape of the NPs (spherical versus rod-like) had a relatively minor impact on their *in vitro* stability. Both spherical and rod-shaped NPs were able to maintain stability under the experimental conditions.

3.3 Assembly mechanisms and molecular docking simulations

Fluorescence intensity and ultraviolet (UV) absorbance spectra of the free CPT solution and each of the NPs were characterized to investigate their assembly mechanisms. As shown in Fig. S5(a) in the ESM, free CPT exhibited the highest fluorescence intensity, while the fluorescence intensity of CPT was significantly reduced in

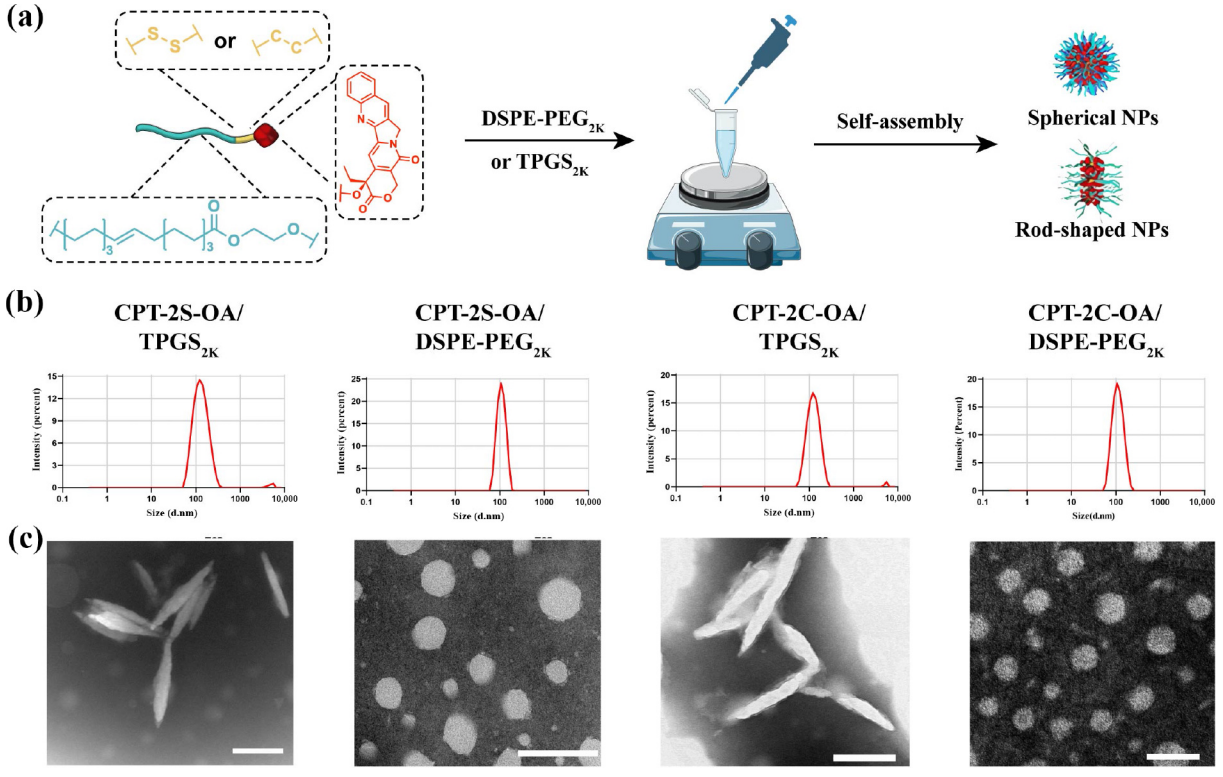

Figure 2 Characterization of prodrug NPs *in vitro*. (a) The preparation method for various formulations. (b) Size distribution of prodrug NPs. (c) TEM images of prodrug NPs. Scale bars: 100 nm.

the NPs formed by the prodrug. This reduction was due to the close stacking of CPT molecules within the NPs, which occurred due to the strong intermolecular interactions among prodrug molecules during NP formation. The decreased intermolecular distance between the planar CPT molecules enhanced π–π interactions, leading to energy transfer in the excited state and thus causing fluorescence quenching. This phenomenon was known as the aggregation-caused quenching (ACQ) effect [28, 29]. In contrast, free CPT molecules maintained a certain distance from one another, resulting in a weaker ACQ effect and a higher fluorescence intensity.

The UV absorbance peak of prodrug NPs exhibited a red shift and broadened compared to free CPT, suggesting the existence of π–π stacking during the assembly process (Fig. S5(b) in the ESM). In addition, to further explore the interactions responsible for self-assembly, the NPs were incubated with various concentrations (10–200 mM) of NaCl, urea, SDS, and KCl, aimed at disrupting electrostatic forces, hydrogen bonding, hydrophobic forces, and π–π stacking, respectively (Fig. S6 in the ESM). SDS considerably increased the size of all NPs and affected their stability, whereas urea had no impact, indicating that hydrophobic forces contributed to the molecular self-assembly. Additionally, the rod-shaped NPs were more sensitive to NaCl and KCl compared to spherical NPs, suggesting that the π–π stacking and electrostatic interactions between CPT and $TPGS_{2K}$ participated in the formation of rod-shaped NPs through enhanced co-assembly force.

Assembly mechanisms of two morphological nanoparticles were investigated by molecular docking analysis. The binding energy between prodrug molecules and PEG was utilized to evaluate the strength of their interactions. In thermodynamic analysis, negative free energy ($\Delta G < 0$) indicates that the assembly process proceeds spontaneously, with lower free energy corresponding to greater stability. The binding energy values were presented as follows (Fig. 3(a)): CPT-2S-OA/$TPGS_{2K}$ (−49.1 kcal/mol), CPT-2C-OA/$TPGS_{2K}$ (−41.4 kcal/mol), CPT-2S-OA/DSPE-PEG_{2K} (−36.5 kcal/mol), CPT-2C-OA/DSPE-PEG_{2K} (−36.1 kcal/mol). The assembly of DSPE-PEG_{2K} with the prodrug occurred via simple plane stacking, resulting in relatively weaker binding. In comparison, $TPGS_{2K}$ could bind more firmly with CPT than DSPE-PEG_{2K}, forming a stable helical molecule structure. These molecular docking results aligned with the conclusions drawn from the self-assembly force analysis, suggesting that the interaction between the benzo-heterocyclic group in $TPGS_{2K}$ and the aromatic rings in CPT may facilitate the formation of a columnar structure.

3.4 Drug release of CPT prodrug nanoparticles

Our previous study demonstrated that disulfide bonds in prodrug NPs could break responsively under high-reduction conditions, thereby releasing CPT to exert its cytotoxic effects (Fig. 3(b)). In contrast, this drug-releasing behavior does not occur in carbon bond-linked NPs due to their lack of reduction sensitivity. To verify the reduction-responsive drug release of prodrug NPs, we evaluated their behavior under different concentrations of DTT, a commonly used analog of glutathione (GSH). The drug release profiles of prodrug NPs in various media are shown in Fig. 3(c). Minimal CPT release (less than 5%) was observed from prodrug NPs in the absence of DTT, indicating limited drug toxicity and side effects during systemic circulation. However, the disulfide bond-linked prodrug NPs demonstrated reduction-responsive drug release. The reduction-triggered CPT release from CPT-2S-OA/DSPE-PEG_{2K} and CPT-2S-OA/$TPGS_{2K}$ was both time- and concentration-dependent. When incubated with 10 mM DTT, both types of disulfide bond-linked prodrug NPs released 95% of CPT within 4 h. As a comparison, the non-sensitive NPs (CPT-2C-OA/$TPGS_{2K}$ and

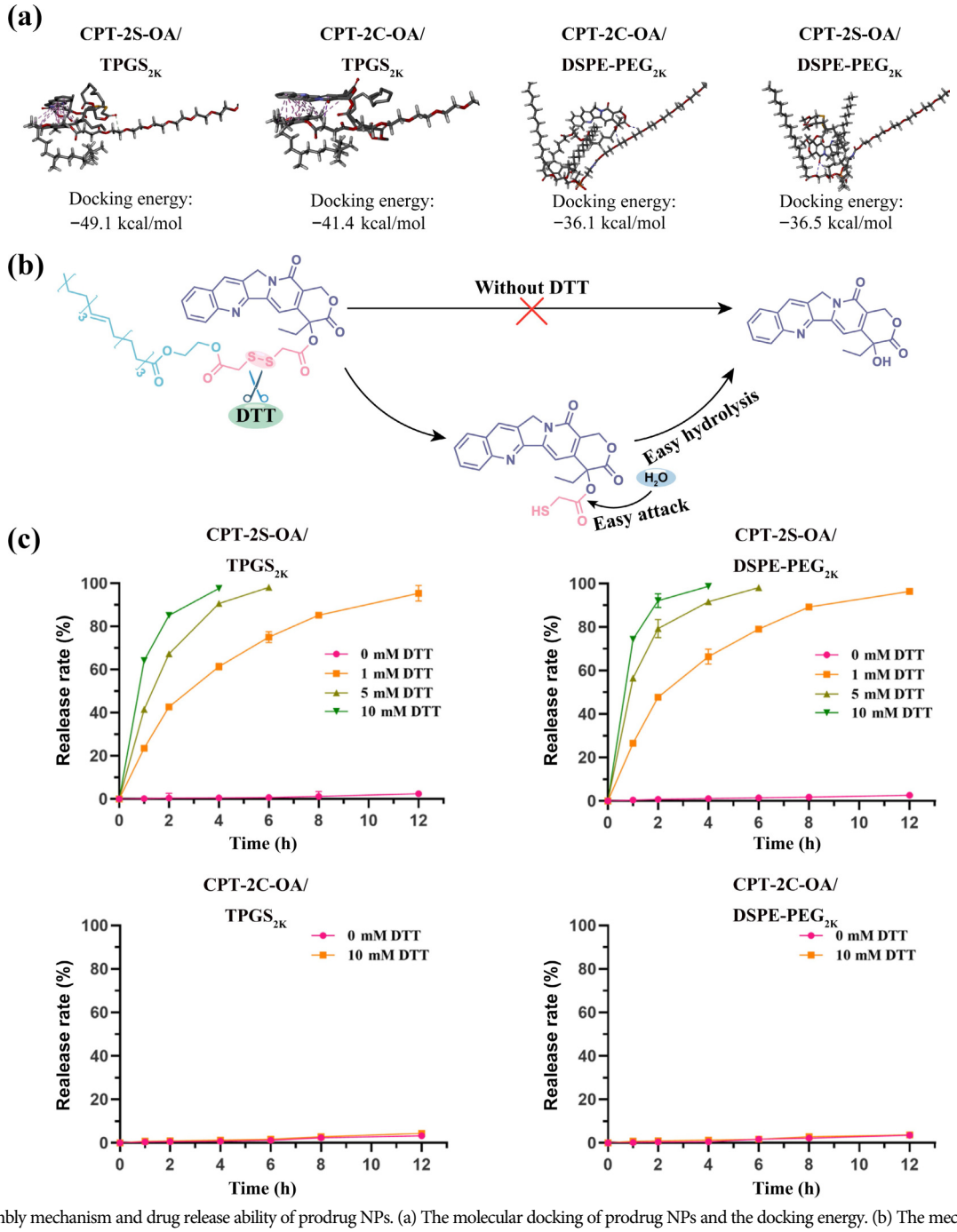

Figure 3 Assembly mechanism and drug release ability of prodrug NPs. (a) The molecular docking of prodrug NPs and the docking energy. (b) The mechanism of DTT-induced reduction-responsive ability of prodrug NPs. (c) Environment-responsive drug release profiles of prodrug NPs.

CPT-2C-OA/DSPE-PEG$_{2K}$) exhibited negligible drug release, regardless of the presence of 1, 5, or 10 mM DTT.

3.5 Cellular uptake and pathways of endocytosis

CT26 cells were incubated with coumarin-6 labeled prodrug NPs for investigating cellular uptake. Compared with free coumarin-6, NPs significantly enhanced fluorescence intensity within cells at both 0.5 and 2 h (Figs. 4(a) and 4(b)). At 2 h, the fluorescence intensity of rod-shaped NPs (CPT-2S-OA/TPGS$_{2K}$ NPs and CPT-2C-OA/TPGS$_{2K}$ NPs) was stronger than that of spherical NPs (CPT-2S-OA/DSPE-PEG$_{2K}$ NPs and CPT-2C-OA/DSPE-PEG$_{2K}$ NPs) under identical experimental conditions.

Further investigation was conducted to elucidate the endocytosis pathways of spherical NPs (CPT-2S-OA/DSPE-PEG$_{2K}$ NPs and CPT-2C-OA/DSPE-PEG$_{2K}$ NPs) and rod-shaped NPs (CPT-2S-OA/TPGS$_{2K}$ NPs and CPT-2C-OA/TPGS$_{2K}$ NPs). The preferred endocytic pathway for these NPs was identified using endocytic inhibition studies. Endocytic inhibitors, CPZ and FLP, were employed to inhibit clathrin-mediated endocytosis and caveolae-mediated endocytosis, respectively. Besides, CT26 cells were incubated at a low temperature (4 °C) to assess the effect of energy on the endocytic process. As shown in Fig. 4(c), the results indicated that after low-temperature treatment, endocytosis of NPs was drastically reduced in all groups, confirming that the

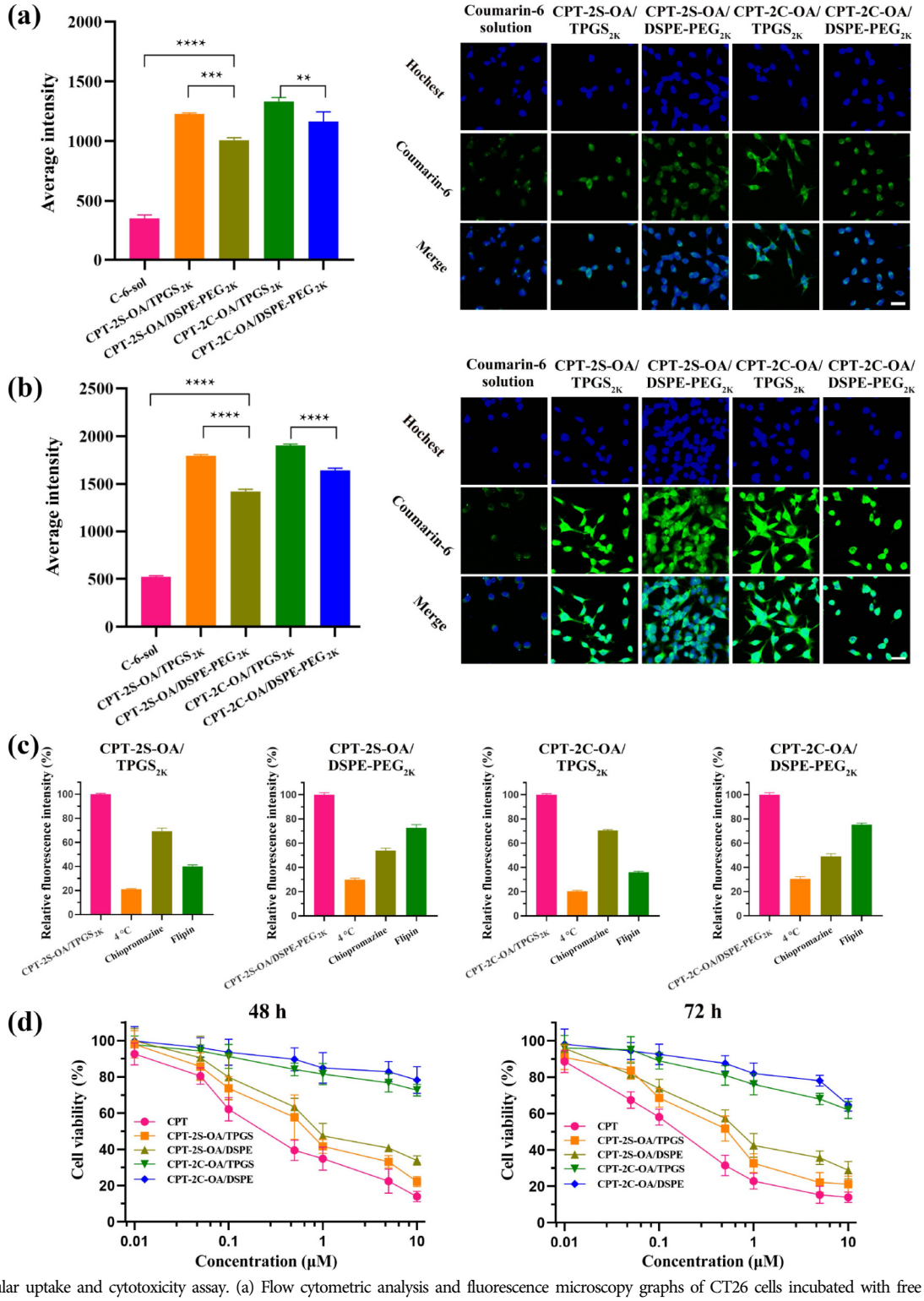

Figure 4 Cellular uptake and cytotoxicity assay. (a) Flow cytometric analysis and fluorescence microscopy graphs of CT26 cells incubated with free coumarin-6 or coumarin-6-labeled formulations for 0.5 h (n = 3). Scale bar:10 μm. (b) Flow cytometric analysis and fluorescence microscopy graphs of CT26 cells incubated with free coumarin-6 or coumarin-6-labeled formulations for 2 h. Scale bar: 10 μm. (c) Flow cytometric analysis of cellular uptake mechanisms of coumarin-6-labeled prodrug NPs (n = 3). (d) *In vitro* cell viability of free CPT and various preparations against CT26 for 48 and 72 h. The data are presented as mean ± SD and were assessed by one-way analysis of variance (ANOVA). $P > 0.05$ (no significance), $0.01 < {}^{*}P < 0.05$, $0.001 < {}^{**}P < 0.01$, $0.0001 < {}^{***}P < 0.001$, and ${}^{****}P < 0.0001$.

endocytosis process is energy-dependent. The internalization of spherical CPT/DSPE-PEG$_{2K}$ NPs predominantly relied on clathrin-mediated endocytosis, whereas the internalization of rod-shaped CPT/TPGS$_{2K}$ NPs was primarily dependent on caveolae-mediated endocytosis. Clathrin is a protein that participates in lysosome membrane recycling. As a result, spherical NPs internalized through clathrin-mediated endocytosis are mainly transported to lysosomes, leading to degradation [30]. In contrast, caveola-

mediated endocytosis bypasses enzymatic degradation, allowing CPT/$TPGS_{2K}$ NPs to be efficiently internalized by tumor cells.

3.6 Cytotoxicity assays

The cytotoxic effects of CPT and prodrug NPs toward CT26 cells (mouse colon carcinoma) were evaluated through MTT assay. The IC_{50} values of CPT and each NP formulation were calculated and summarized in Table S2 in the ESM. The cell viability profiles were illustrated in Fig. 4(d). Compared with the CPT solution, the prodrug NPs showed lower cytotoxicity, attributed to the delayed release of CPT. The cytotoxicity of formulations followed the sequence: CPT-2S-OA/$TPGS_{2K}$ NPs > CPT-2S-OA/DSPE-PEG_{2K} NPs > CPT-2C-OA/$TPGS_{2K}$ NPs > CPT-2C-OA/DSPE-PEG_{2K} NPs. In comparison with the disulfide bond-bridged prodrug NPs, CPT release from CPT-2C-OA/$TPGS_{2K}$ NPs and CPT-2C-OA/DSPE-PEG_{2K} NPs was minimal, corresponding to their lower rates of proliferation inhibition. CPT-2S-OA/$TPGS_{2K}$ NPs exhibited stronger cytotoxicity than CPT-2S-OA/DSPE-PEG_{2K} NPs with similar release profiles, agreeing well with the cellular uptake results.

3.7 Pharmacokinetics

The pharmacokinetic profiles of various preparations were evaluated in Sprague-Dawley rats. The plasma concentration-time curves and the pharmacokinetic parameters of each group were presented in Fig. 5(a) and Table. S3 in the ESM. While the CPT solution was promptly cleared from the blood, the prodrug NPs exhibited significantly longer circulation times. The area under the curve (AUC) of CPT-2S-OA/$TPGS_{2K}$ NPs, CPT-2S-OA/DSPE-PEG_{2K} NPs, CPT-2C-OA/$TPGS_{2K}$ NPs, and CPT-2C-OA/DSPE-PEG_{2K} NPs, including prodrug and free drug, were approximately 21.8-, 11.4-, 10.4- and 7.5-times higher than that of the CPT solution, respectively. Notably, compared to spherical NPs (CPT-2S-OA/DSPE-PEG_{2K}), rod-shaped NPs (CPT-2S-OA/$TPGS_{2K}$) exhibited larger AUC values, indicating they could maintain higher exposure *in vivo*. This increase can be attributed to the enhanced planar interactions between drug molecules and the stabilizer $TPGS_{2K}$ within the rod-shaped particles, which facilitated the maintenance of the nanostructure in the bloodstream. In addition, existing literature suggested that rod-shaped NPs exhibit altered hydrodynamic behavior in blood vessels compared to spherical particles. This change helped rod-shaped NPs avoid phagocytosis by the reticuloendothelial system, thereby contributing to prolonged circulation times of the nanodrug in the bloodstream [31]. In comparison to CPT-2S-OA NPs, CPT-2C-OA NPs with the same shape had a lower AUC value, likely due to their reduced colloidal stability (Fig. S4 in the ESM).

3.8 *In vivo* biodistribution

For evaluating the biodistribution, CT26 tumor-bearing BALB/c mice were intravenously administrated with DiR solution and DiR-labeled prodrug NPs. As shown in Figs. 5(b)–5(d), the fluorescence of the DiR solution was primarily detected in the liver, lung, and spleen. In contrast, prodrug NPs exhibited significantly higher concentrations in the tumor than the DiR solution, indicating that the enhanced permeability and retention (EPR) effect facilitated greater tumor accumulation of prodrug NPs. Furthermore, compared with the spherical prodrug NPs (CPT-2S-OA/DSPE-PEG_{2K} NPs and CPT-2C-OA/DSPE-PEG_{2K} NPs), the rod-like

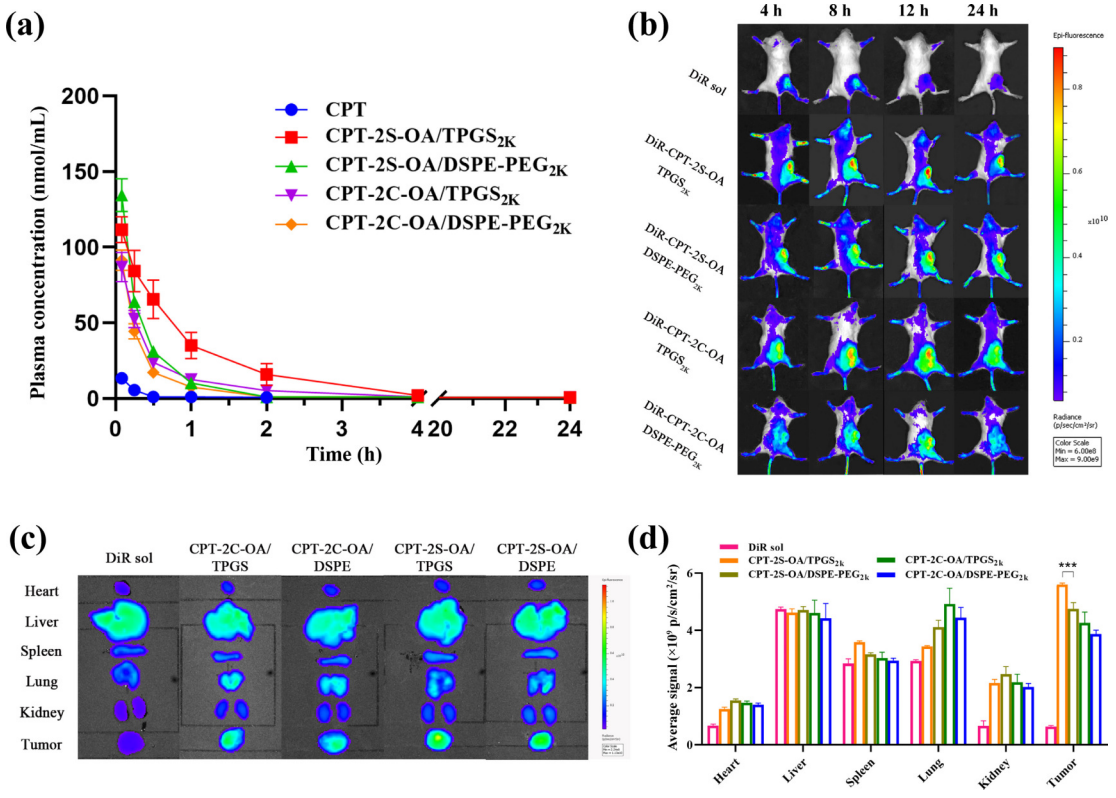

Figure 5 Pharmacokinetics and *in vivo* biodistribution. (a) *In vivo* plasma concentration-time profiles of CPT and prodrug NPs. Data are shown as mean ± SD (n = 3). (b) Optical imaging of DiR solution and DiR-labeled prodrug NPs for 4, 8, 12, and 24 h. The excitation wavelength is set to 748 nm before obtaining the fluorescence pictures. (c) *In vitro* fluorescence imaging and (d) quantitative analysis of major organs and tumors at 24 h post-injection (n = 3). The data are presented as means ± SD and were assessed by one-way analysis of variance (ANOVA). $P > 0.05$ (no significance), $0.01 < {}^{*}P < 0.05$, $0.001 < {}^{**}P < 0.01$, $0.0001 < {}^{***}P < 0.001$, and ${}^{****}P < 0.0001$.

prodrug NPs (CPT-2S-OA/TPGS$_{2K}$ NPs and CPT-2C-OA/TPGS$_{2K}$ NPs) demonstrated improved tumor accumulation due to their prolonged circulation time and higher cellular uptake efficiency.

As shown in Fig. S7 in the ESM, fluorescence imaging of tumor sections revealed that, following intravenous injection, the fluorescence of free CPT was primarily localized at the tumor periphery, suggesting limited penetration through the dense extracellular matrix into the tumor core. This limited distribution can be attributed to the rapid plasma clearance and reduced tumor accumulation of the free drug *in vivo*. In contrast, the shape of nanoassemblies appeared to influence tumor penetration. Rod-shaped NPs showed a more uniform fluorescence distribution throughout the tumor tissue compared to spherical particles, indicating enhanced penetration capability. This difference may be due to the greater deformability of nanorods, which potentially improved their circulation time *in vivo* and facilitated their passage across physiological barriers [19, 32].

3.9 *In vivo* antitumor efficacy

The antitumor effects of prodrug NPs and CPT were investigated following intravenous administration when the tumor volume reached approximately 100 mm^3 (Fig. 6(a)). As shown in Figs. 6(b) and 6(c), the tumor volume in mice treated with non-sensitive CPT-2C-OA/TPGS$_{2K}$ NPs and CPT-2C-OA/DSPE-PEG$_{2K}$ NPs increased rapidly, likely due to insufficient drug release from the prodrugs. In contrast, CPT-2S-OA/TPGS$_{2K}$ NPs and CPT-2S-OA/DSPE-PEG$_{2K}$ NPs exhibited stronger antitumor activity compared to CPT. Furthermore, the tumor-inhibiting effect of CPT-2S-OA/TPGS$_{2K}$ NPs was superior to that of CPT-2S-OA/DSPE-PEG$_{2K}$ NPs, which may be attributed to the improved plasma stability, prolonged circulation time, and higher cellular uptake efficiency of rod-shaped NPs. The TUNEL assay was used to assess cellular apoptosis following treatment. As shown in Fig. S8 in the ESM, tumors treated with CPT-2S-OA/TPGS$_{2K}$ NPs displayed more extensive apoptosis, indicating potent antitumor efficacy. In addition, TUNEL-stained tumor slices revealed widespread tumor necrosis (Fig. S8 in the ESM).

During the treatment period, no significant changes in body weight were observed in any of the treatment groups (Fig. 6(d)). After the experiment, examinations of hepatic and renal function showed no abnormalities, and no significant histological damage was observed in the H&E-stained tissue slices of vital organs (Fig.

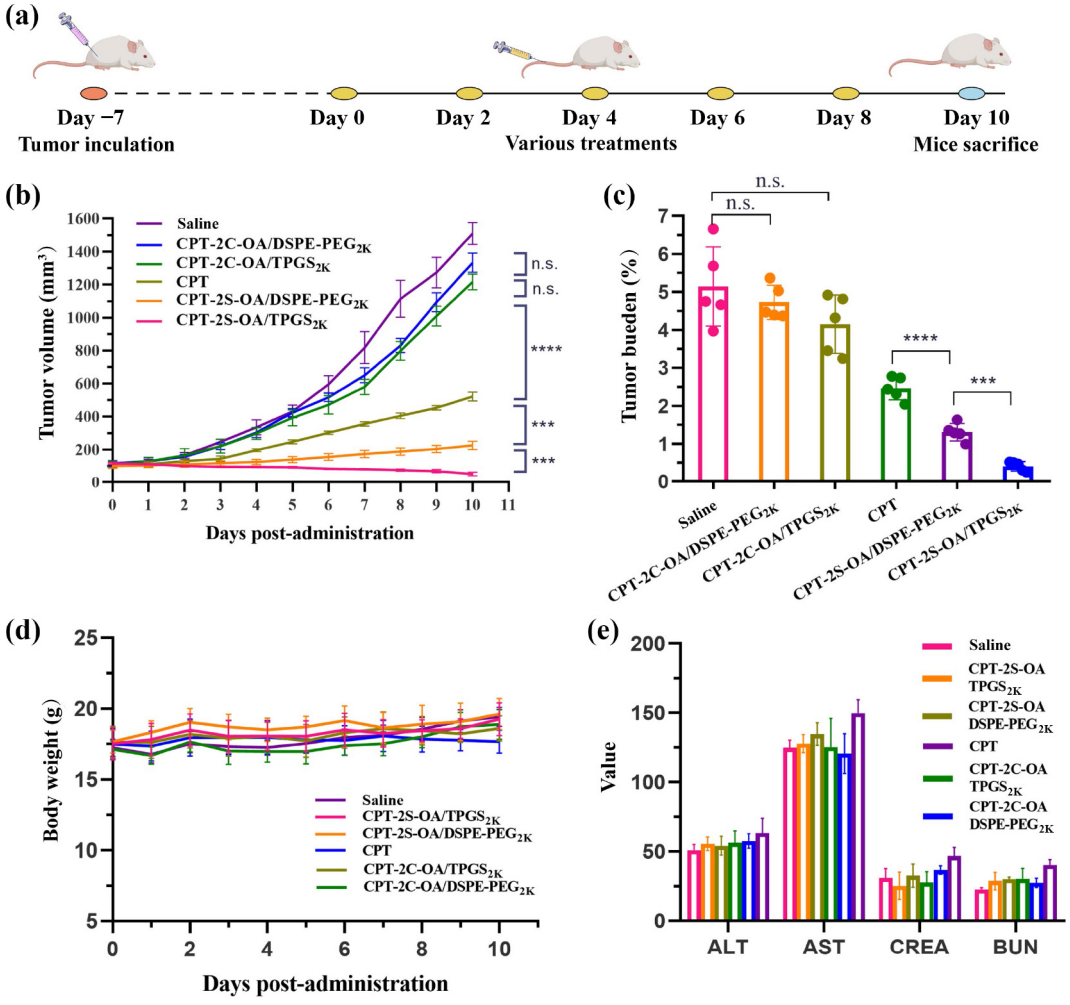

Figure 6 *In vivo* antitumor ability and biosecurity of each formulation. (a) Schematic diagram of the antitumor efficacy study in BALB/c mice. (b) Tumor volume profiles treated with different formulations. (c) Tumor burden after the final administration. (d) Body weight record. (e) Hepatorenal function parameters after the final administration. AST: aspartate aminotransferase (U/L), ALT: alanine aminotransferase (U/L), BUN: blood urea nitrogen (mmol/L), CREA: creatinine (μmol/L). The data are presented as mean ± SD (n = 5) and were assessed by one-way analysis of variance (ANOVA). $P > 0.05$ (no significance), $0.01 < {}^{*}P < 0.05$, $0.001 < {}^{**}P < 0.01$, $0.0001 < {}^{***}P < 0.001$, and ${}^{****}P < 0.0001$.

6(e), and Fig. S9 in the ESM). Each group of prodrug NPs demonstrated biological safety, and no notable nonspecific toxicity was detected in major organs.

4 Conclusions

In this study, we designed and prepared two types of prodrug NPs with distinct morphology and investigated the driving forces behind their co-assembly, as well as how these shapes influenced intracellular behavior, biodistribution, and antitumor efficiency. Hydrophobic forces were involved in both types of co-assembly; however, π–π stacking and electrostatic interactions likely contributed to the formation of rod-shaped NPs by enhancing the co-assembly forces. The endocytosis of rod-shaped NPs primarily relied on caveolae-mediated pathways rather than clathrin-mediated ones, which could help avoid lysosomal degradation and improve cellular uptake efficiency. Compared to DSPE-PEG_{2K}-modified nanospheres, $TPGS_{2K}$-modified rod-like prodrug NPs demonstrated higher cytotoxicity, prolonged circulation time, and enhanced tumor accumulation, all of which contributed to increased antitumor activity. Our study on rod-like NPs highlighted that biological geometry significantly influenced *in vivo* transport and tumor targeting capabilities. This finding provided new insights into the design of morphology-based, environment-responsive DDS to further optimize antitumor therapy efficiency.

Electronic Supplementary Material: Supplementary material (synthetic route, structure confirmation, colloidal stability, fluorescence spectra, UV absorption spectra, assembly mechanisms study, tumor sections and summary tables) is available in the online version of this article at https://doi.org/10.26599/NR.2025.94907177.

Acknowledgements

This research was supported by National Natural Science Foundation of China (Nos. 82273874 and 82404561), Liaoning Revitalization Talents Program (No. XLYC22202019), the China National Postdoctoral Program for Innovative Talents (No. BX20240233), the Postdoctoral Fellowship Program (Grade B) of China Postdoctoral Science Foundation (No. GZB20240179), the China Postdoctoral Science Foundation (No. 2023MD744230), Doctoral Scientific Research Launching Fund Project of Liaoning province (No. 2024-BS-075), and Prospective Basic research project of 2024 Scientific Research Project of Liaoning Department of Education (No. LJ212410163042).

Data availability

All data needed to support the conclusions in the paper are presented in the manuscript and the Electronic Supplementary Material.

Declaration of competing interest

The authors declare no competing interests in this paper.

Author contribution statement

F. X. L., R. Z. L., K. Y. W., and J. S. conceived the project and design experiments. F. X. L., R. Z. L., X. W., X. K., and H. T. Z. performed the experiments. R. Z. L. and K. Y. W. analyzed the results. Y. X. Y., H. N. Z., Q. M. K., Z. G. H., and S. Z. Z. provided useful suggestions. F. X. L., R. Z. L., and J. S. wrote the manuscript. X. Y. F., J. C., and H. Y. revised the manuscript. All authors have approved the final version of the manuscript.

Informed consent

Not applicable.

Ethics statement

All the animal experiments were conducted according to the Guidelines for the Care and Use of Laboratory Animals and received ethical approval from the Institutional Animal Ethical Care Committee (IAEC) of Shenyang Pharmaceutical University (No. SYPU-IACUC-C2021-12-3-206).

Use of AI statement

None.

References

[1] Chabner, B. A.; Roberts, T. G. Jr. *Chemotherapy and the war on cancer. Nat. Rev. Cancer* **2005**, *5*, 65–72.

[2] Zhang, X. B.; Xiong, J. C.; Wang, K. Y.; Yu, H.; Sun, B. J.; Ye, H.; Zhao, Z. Q.; Wang, N.; Wang, Y. Q.; Zhang, S. W. et al. Erythrocyte membrane-camouflaged carrier-free nanoassembly of FRET photosensitizer pairs with high therapeutic efficiency and high security for programmed cancer synergistic phototherapy. *Bioact. Mater.* **2021**, *6*, 2291–2302.

[3] Huang, M.; Lu, J. J.; Ding, J. Natural products in cancer therapy: Past, present and future. *Nat. Prod. Bioprospect.* **2021**, *11*, 5–13.

[4] Tang, Z.; Yin, L. N.; Zhang, Y. W.; Yu, W. Y.; Wang, Q.; Zhan, Z. L. Preparation and study of two kinds of ophthalmic nano-preparations of everolimus. *Drug Deliv.* **2019**, *26*, 1235–1242.

[5] Wang, K. Y.; Ye, H.; Zhang, X. B.; Wang, X.; Yang, B.; Luo, C.; Zhao, Z. Q.; Zhao, J.; Lu, Q.; Zhang, H. T. et al. An exosome-like programmable-bioactivating paclitaxel prodrug nanoplatform for enhanced breast cancer metastasis inhibition. *Biomaterials* **2020**, *257*, 120224.

[6] Ye, H.; Wang, K. Y.; Lu, Q.; Zhao, J.; Wang, M. L.; Kan, Q. M.; Zhang, H. T.; Wang, Y. J.; He, Z. G.; Sun, J. Nanosponges of circulating tumor-derived exosomes for breast cancer metastasis inhibition. *Biomaterials* **2020**, *242*, 119932.

[7] Ye, H.; Wang, K. Y.; Wang, M. L.; Liu, R. Z.; Song, H.; Li, N.; Lu, Q.; Zhang, W. J.; Du, Y. Q.; Yang, W. Q. et al. Bioinspired nanoplatelets for chemo-photothermal therapy of breast cancer metastasis inhibition. *Biomaterials* **2019**, *206*, 1–12.

[8] Li, G. T.; Sun, B. J.; Li, Y. Q.; Luo, C.; He, Z. G.; Sun, J. Small-molecule prodrug nanoassemblies: An emerging nanoplatform for anticancer drug delivery. *Small* **2021**, *17*, 2101460.

[9] Li, S. M.; Shan, X. Z.; Wang, Y. Q.; Chen, Q.; Sun, J.; He, Z. G.; Sun, B. J.; Luo, C. Dimeric prodrug-based nanomedicines for cancer therapy. *J. Controlled Release* **2020**, *326*, 510–522.

[10] Sun, B. J.; Luo, C.; Zhang, X. B.; Guo, M. R.; Sun, M. C.; Yu, H.; Chen, Q.; Yang, W. Q.; Wang, M. L.; Zuo, S. Y. et al. Probing the impact of sulfur/selenium/carbon linkages on prodrug nanoassemblies for cancer therapy. *Nat. Commun.* **2019**, *10*, 3211.

[11] Wang, Y. L.; Wang, J. M.; Yang, L. Y.; Wei, W.; Sun, B. J.; Na, K. X.; Song, Y. X.; Zhang, H. T.; He, Z. G.; Sun, J. et al. Redox dual-responsive paclitaxel-doxorubicin heterodimeric prodrug self-delivery nanoaggregates for more effective breast cancer synergistic

combination chemotherapy. *Nanomed.: Nanotechnol. Biol. Med.* **2019**, *21*, 102066.
[12] Luo, C.; Sun, B. J.; Wang, C.; Zhang, X. B.; Chen, Y.; Chen, Q.; Yu, H.; Zhao, H. Q.; Sun, M. C.; Li, Z. B. et al. Self-facilitated ROS-responsive nanoassembly of heterotypic dimer for synergistic chemo-photodynamic therapy. *J. Controlled Release* **2019**, *302*, 79–89.
[13] Zuo, S. Y.; Sun, B. J.; Yang, Y. X.; Zhou, S.; Zhang, Y.; Guo, M. R.; Sun, M. C.; Luo, C.; He, Z. G.; Sun, J. Probing the superiority of diselenium bond on docetaxel dimeric prodrug nanoassemblies: Small roles taking big responsibilities. *Small* **2020**, *16*, 2005039.
[14] Jiang, M. J.; Mu, J.; Jacobson, O.; Wang, Z. T.; He, L. C.; Zhang, F. W.; Yang, W. J.; Lin, Q. Y.; Zhou, Z. J.; Ma, Y. et al. Reactive oxygen species activatable heterodimeric prodrug as tumor-selective nanotheranostics. *ACS Nano* **2020**, *14*, 16875–16886.
[15] Chen, X.; Lei, S.; Lin, J.; Huang, P. Stimuli-responsive image-guided nanocarriers as smart drug delivery platforms. *Expert Opin. Drug Deliv.* **2022**, *19*, 1487–1504.
[16] Zhang, X. B.; Li, N.; Zhang, S. W.; Sun, B. J.; Chen, Q.; He, Z. G.; Luo, C.; Sun, J. Emerging carrier-free nanosystems based on molecular self-assembly of pure drugs for cancer therapy. *Med. Res. Rev.* **2020**, *40*, 1754–1775.
[17] Luo, C.; Sun, J.; Sun, B. J.; Liu, D.; Miao, L.; Goodwin, T. J.; Huang, L.; He, Z. G. Facile fabrication of tumor redox-sensitive nanoassemblies of small-molecule oleate prodrug as potent chemotherapeutic nanomedicine. *Small* **2016**, *12*, 6353–6362.
[18] Luo, C.; Sun, J.; Liu, D.; Sun, B. J.; Miao, L.; Musetti, S.; Li, J.; Han, X. P.; Du, Y. Q.; Li, L. et al. Self-assembled redox dual-responsive prodrug-nanosystem formed by single thioether-bridged paclitaxel-fatty acid conjugate for cancer chemotherapy. *Nano Lett.* **2016**, *16*, 5401–5408.
[19] Chauhan, V. P.; Popović, Z.; Chen, O.; Cui, J.; Fukumura, D.; Bawendi, M. G.; Jain, R. K. Fluorescent nanorods and nanospheres for real-time *in vivo* probing of nanoparticle shape-dependent tumor penetration. *Angew. Chem., Int. Ed.* **2011**, *50*, 11417–11420.
[20] Fan, M. M.; Zhang, W. Z.; Cheng, C.; Liu, Y.; Li, B. J.; Sun, X.; Zhang, S. Evaluation of rod-shaped nanoparticles as carriers for gene delivery. *Part. Part. Syst. Charact.* **2014**, *31*, 994–1000.
[21] Agarwal, R.; Singh, V.; Jurney, P.; Shi, L.; Sreenivasan, S. V.; Roy, K. Mammalian cells preferentially internalize hydrogel nanodiscs over nanorods and use shape-specific uptake mechanisms. *Proc. Natl. Acad. Sci. USA* **2013**, *110*, 17247–17252.
[22] Barua, S.; Yoo, J. W.; Kolhar, P.; Wakankar, A.; Gokarn, Y. R.; Mitragotri, S. Particle shape enhances specificity of antibody-displaying nanoparticles. *Proc. Natl. Acad. Sci. USA* **2013**, *110*, 3270–3275.
[23] Li, D.; Li, X.; Bai, J.; Liu, Y.; de Vries, R.; Li, Y. Rod-shaped polypeptide nanoparticles for siRNA delivery. *Int. J. Biol. Macromol.* **2021**, *166*, 401–408.
[24] Zhao, Z. M.; Ukidve, A.; Krishnan, V.; Mitragotri, S. Effect of physicochemical and surface properties on *in vivo* fate of drug nanocarriers. *Adv. Drug Delivery Rev.* **2019**, *143*, 3–21.
[25] Decuzzi, P.; Godin, B.; Tanaka, T.; Lee, S. Y.; Chiappini, C.; Liu, X.; Ferrari, M. Size and shape effects in the biodistribution of intravascularly injected particles. *J. Controlled Release* **2010**, *141*, 320–327.
[26] Zhang, X. B.; Sun, B. J.; Zuo, S. Y.; Chen, Q.; Gao, Y. L.; Zhao, H. Q.; Sun, M. C.; Chen, P. Y.; Yu, H.; Zhang, W. J. et al. Self-assembly of a pure photosensitizer as a versatile theragnostic nanoplatform for imaging-guided antitumor photothermal therapy. *ACS Appl. Mater. Interfaces* **2018**, *10*, 30155–30162.
[27] Li, L. X.; Liu, T.; Zuo, S. Y.; Li, Y. Q.; Zhao, E. W.; Lu, Q.; Wang, D. P.; Sun, Y. X.; He, Z. G.; Sun, B. J. et al. Satellite-type sulfur atom distribution in trithiocarbonate bond-bridged dimeric prodrug nanoassemblies: Achieving both stability and activatability. *Adv. Mater.* **2024**, *36*, 2310633.
[28] Zhao, D. Y.; Tao, W. H.; Li, S. H.; Chen, Y.; Sun, Y. H.; He, Z. G.; Sun, B. J.; Sun, J. Apoptotic body-mediated intercellular delivery for enhanced drug penetration and whole tumor destruction. *Sci. Adv.* **2021**, *7*, eabg0880.
[29] Yang, Y. X.; Sun, B. J.; Zuo, S. Y.; Li, X. M.; Zhou, S.; Li, L. X.; Luo, C.; Liu, H. Z.; Cheng, M. S.; Wang, Y. J. et al. Trisulfide bond-mediated doxorubicin dimeric prodrug nanoassemblies with high drug loading, high self-assembly stability, and high tumor selectivity. *Sci. Adv.* **2020**, *6*, eabc1725.
[30] Mao, Y. L.; Feng, S.; Li, S.; Zhao, Q. F.; Di, D. H.; Liu, Y. F.; Wang, S. L. Chylomicron-pretended nano-bio self-assembling vehicle to promote lymphatic transport and GALTs target of oral drugs. *Biomaterials* **2019**, *188*, 173–186.
[31] Tan, J.; Lu, Y. C.; Xu, J. H.; Luo, G. S. Modeling investigation of mass transfer of gas-liquid concurrent flow processes. *Sep. Purif. Technol.* **2013**, *109*, 77–86.
[32] Agarwal, R.; Jurney, P.; Raythatha, M.; Singh, V.; Sreenivasan, S. V.; Shi, L.; Roy, K. Effect of shape, size, and aspect ratio on nanoparticle penetration and distribution inside solid tissues using 3D spheroid models. *Adv. Healthcare Mater.* **2015**, *4*, 2269–2280.